GEOPHYSICS, VOL. 81, NO. 5 (SEPTEMBER-OCTOBER 2016); P. U51–U60, 8 FIGS., 4 TABLES.
10.1190/GEO2015-0438.1

Seismic velocity inversion for patchy and homogeneous fluid-distribution conditions in shallow, unconsolidated sands

Jie Shen[1] and Juan M. Lorenzo[2]

ABSTRACT

Knowledge of homogeneous and heterogeneous fluid-distribution conditions in unconsolidated sediments is important for the selection of remediation techniques for groundwater contamination. However, for unconsolidated sediments, fluid-distribution conditions from laboratory tests on core samples may not be representative of in situ conditions. We have developed a seismic inversion method to determine in situ fluid-distribution conditions that involves inverting experimental seismic P- and S-wave velocities using Hertz-Mindlin and Biot-Gassmann models with different averaging methods (Wood and Hill averages) and different fluid-distribution condition assumptions. This method can determine whether seismic velocity-versus-depth profiles are better explained assuming heterogeneous or homogeneous saturation conditions in shallow (<1 m depth) unconsolidated sands. During the imbibition and drainage of shallow unconsolidated sands, we have observed nonmonotonic relationships between P-wave velocity and water levels (WLs) as well as an S-wave velocity and WLs that were consistent with other field and laboratory observations. This relationship can be explained by transitions between the lower Wood bound and the higher Hill bound. The transition is possibly caused by the alternation in the size of fluid patches between small and large during the imbibition and drainage. Inverted results can be verified by a good correlation (difference <7%) between the inverted and measured water saturation using moisture sensors.

INTRODUCTION

Partially saturated unconsolidated sediments contain a mixture of two or more fluids that can be distributed either homogeneously or heterogeneously (in patches). However, the commonly applied laboratory ultrasonic core tests for identifying fluid distributions are costly and may not represent in situ conditions because of the disturbance of unconsolidated samples during core transportation, and the scaling issues with translating between ultrahigh frequencies commonly used in laboratory studies and lower frequencies used in the field (Cadoret et al., 1995; Toms-Stewart et al., 2009). During field tidal water-level (WL) change experiments (Bachrach and Nur, 1998) and laboratory WL change experiments (Velea et al., 2000; Lorenzo et al., 2013), changes in WL and water saturation S_w lead to unexpected alternations of the fast P-wave velocity V_P between increasing and decreasing trends. There is a lack of understanding of these observed nonmonotonic V_P-WL and V_P-S_w relationships. Determining the saturation condition can help to select an adequate remediation technique for groundwater contamination based on whether the contaminants occur in patches or homogeneously (Dvorkin and Nur, 1998).

In this paper, we propose a seismic inversion workflow to determine in situ fluid-distribution conditions, by minimizing the difference between experimental and predicted velocity-versus-depth profiles. The predicted velocity-versus-depth profiles are calculated from rock-physics models with assumptions of either heterogeneous or homogeneous saturation conditions. For the inversion, we acquire the following experimental data: P- and S-wave velocity-versus-depth profiles from a seismic survey and water saturation-versus-depth profiles from electrical measurements. Our inversion results can indicate that the fluid-distribution condition can be either homogeneous or heterogeneous. We can also differentiate large- or small-sized patches from our inversion. Small-sized patches are possibly caused by pore-size heterogeneity, and the large-sized patches

Manuscript received by the Editor 19 August 2015; revised manuscript received 9 March 2016; published online 7 July 2016.
[1]Formerly Louisiana State University, Department of Geology & Geophysics, Baton Rouge, Louisiana, USA; presently Shell Exploration & Production Company, New Orleans, Louisiana, USA. E-mail: bjshenjie@gmail.com.
[2]Louisiana State University, Department of Geology & Geophysics, Baton Rouge, Louisiana, USA. E-mail: gllore@lsu.edu.

may be caused by material property heterogeneity. The inversion results indicate that the nonmonotonic V_P-WL and V_P-S_w relationships are attributable to the variation in fluid-distribution conditions, and V_P changes can be interpreted with transitions between the Hertz-Mindlin-Biot-Gassmann-Wood (HM-BG-Wood) bound and the Hertz-Mindlin-Biot-Gassmann-Hill (HM-BG-Hill) bound with the change in the size of patches.

The concept of the homogeneous or heterogeneous (patchy) fluid-distribution condition can be understood with the soil-water characteristic curve (SWCC) (Dvorkin and Nur, 1998), which shows the relationship between saturation and capillary head (or capillary pressure) (van Genuchten, 1980):

$$S_e = \left[\frac{1}{1 + [ah_c]^n}\right]^m, \tag{1}$$

where S_e is the effective water saturation; h_c is the capillary head; and a, n, and m are the empirical fitting parameters corresponding to various sediment properties. If the fluid-distribution condition is homogeneous, the fluid is evenly distributed in the pore space, and the water saturation is constant within the sediment volume for a given capillary head. In contrast, if the fluid-distribution condition is heterogeneous, the saturation within the patches (the relatively smaller zones) is higher or lower than the saturation within the surrounding area at a fixed capillary head (Dvorkin and Nur, 1998). The SWCC within the patches is different than the curve within the adjacent area, depending on the heterogeneity in the sediment properties, such as porosity and permeability (Knight et al., 1998), interfacial tension, and wettability conditions (Riaz et al., 2007).

For unsaturated sediments, the forces governing two-phase fluid flow during imbibition and drainage are capillary, gravitational, and viscous forces (Løvoll et al., 2005; Riaz et al., 2007). Viscous forces can be negligible in an air-water system in which the viscosities of the wetting (water) and nonwetting (air) fluids are very different because residual air offers very little resistance to water flow (Lopes et al., 2014). Gravitational and capillary forces determine the saturation characteristics. Gravitational forces pull water downward, whereas capillary forces drag and hold water in the pore spaces. Capillary forces decrease as water saturation increases, and vice versa. At the beginning of imbibition, water saturation is lowest, capillary pressure is highest, and finger-shaped wetting fronts (so-called capillary fingers) are created that rise along with the water table. As water saturation increases, capillary pressure aids in redistribution of water from large pores to surrounding small pores (Lopes et al., 2014). During drainage, gravitational forces dominate initially until water drains to a low enough level that capillary pressure reaches equilibrium with gravitational forces, and drainage stops (DiCarlo, 2003).

Velocity models that are applied in our inversion (Shen et al., 2015) are based on the commonly accepted Hertz-Mindlin (Hertz, 1882; Mindlin, 1949) and Biot-Gassmann (Gassmann, 1951; Biot, 1962) (HM-BG) theories, but with different averaging methods depending on the patch size. When the patch size is small compared with the diffusion length, an average fluid bulk modulus can be given by the Wood (1941) average, which uses a weighted harmonic mean of the bulk modulus of each pore fluid. The diffusion length mainly relates to rock permeability, fluid viscosity, and wave frequency ($\lambda = \sqrt{D/\omega}$, where λ is the diffusion length, ω is the angular wave frequency, $D = \kappa K_{\mathrm{fl}}/\eta\phi$ is the diffusivity, κ is the permeability, η is the fluid viscosity, K_{fl} is the fluid bulk modulus, and ϕ is the porosity) (Norris, 1993). Applying the average fluid bulk modulus from the Wood average with the HM-BG theories, the HM-BG-Wood model is valid to determine the lower bound of seismic velocity (Müller et al., 2010). In contrast, if the patch size is much larger than the diffusion length, the average effective elasticity can be determined with the Hill (1963) average by using a weighted harmonic mean of the effective bulk and shear moduli of each patch (Müller et al., 2010). Applying the average effective elasticity from the Hill average with the HM-BG theories, the HM-BG-Hill model predicts the upper bound of seismic velocity. The HM-BG-Wood and HM-BG-Hill bounds describe seismic velocity in the softest and the stiffest material, respectively (Mavko et al., 2009).

The observed fast P-wave seismic velocity and water saturation V_P-S_w relationships vary between different laboratory imbibition and drainage tests of limestone and sandstone core samples (Murphy, 1982; Knight and Nolen-Hoeksema, 1990; Cadoret et al., 1995, 1998; Knight et al., 1998; Monsen and Johnstad, 2005; Lebedev et al., 2009). The different observations are attributed to the differences in sediment heterogeneity and experiment setup (e.g., seismic frequency, injection rate, and the density and viscosity of pore fluids) (Homsy, 1987). Some observations show that the experimental V_P-S_w relationship can be explained by the lower velocity bound from the HM-BG-Wood model during imbibition, and the upper velocity bound from the HM-BG-Hill model during drainage (Murphy, 1982; Knight and Nolen-Hoeksema, 1990; Cadoret et al., 1995; Monsen and Johnstad, 2005;). However, other experiments show a nonmonotonic V_P-S_w relationship that can be explained by the transitions between the HM-BG-Wood and the HM-BG-Hill bounds, depending on the change in patch size (Lebedev et al., 2009) and seismic frequency (Cadoret et al., 1995). During injection of water into a sandstone sample, Lebedev et al. (2009) observe that V_P decreases slightly and follows the HM-BG-Wood bound at low water saturations. When water saturation exceeds 40%, V_P sharply increases and can be interpreted by a transition from the HM-BG-Wood to HM-BG-Hill bound. Their results from X-ray computer tomography show that the interpreted transition from the HM-BG-Wood to HM-BG-Hill bound corresponds to the clustering of small fluid patches and the formation of larger patches.

The Hertz-Mindlin and Biot-Gassmann theories

In the HM-BG model, P-wave V_P and S-wave velocities V_S are calculated from the effective bulk modulus, shear modulus, and density (Mavko et al., 2009):

$$V_P = \sqrt{\frac{K_{\mathrm{eff}} + \frac{4}{3}G_{\mathrm{eff}}}{\rho_{\mathrm{bulk}}}}, \tag{2}$$

$$V_S = \sqrt{\frac{G_{\mathrm{eff}}}{\rho_{\mathrm{bulk}}}}, \tag{3}$$

where K_{eff} and G_{eff} are the effective bulk and shear moduli, respectively, and ρ_{bulk} is the bulk density of the sand matrix with pore fluids:

$$\rho_{\mathrm{bulk}} = \phi(S_w\rho_{\mathrm{water}} + (1 - S_w)\rho_{\mathrm{air}}) + (1 - \phi)\rho_0, \tag{4}$$

where ϕ is the porosity of the skeletal matrix, S_w is the water saturation (the degree of saturation), ρ_{water} is the density of water, ρ_{air} is the density of air, and ρ_0 is the grain density.

Biot-Gassmann fluid substitution theory estimates effective bulk and shear moduli (equations 2 and 3) of the sand matrix and accounts for pore fluids (Mavko et al., 2009):

$$K_{eff} = \frac{K_0\left(\frac{K_m}{K_0-K_m} + \frac{K_{fl}}{\phi(K_0-K_{fl})}\right)}{1 + \frac{K_m}{K_0-K_m} + \frac{K_{fl}}{\phi(K_0-K_{fl})}}, \quad (5)$$

$$G_{eff} = G_m, \quad (6)$$

where K_0 is the bulk modulus of the sand grains, K_m is the bulk modulus of the "dry" sand matrix, G_m is the shear modulus of the "dry" sand matrix, and K_{fl} is the bulk modulus of the pore fluids.

The matrix elastic moduli (equations 5 and 6) can be estimated using Hertz-Mindlin contact theory by assuming the sand grains are a pack of identical spheres (Mavko et al., 2009):

$$K_m = \sqrt[3]{\frac{C^2(1-\phi)^2 G_0^2}{18\pi^2(1-\nu)^2} P_{eff}}, \quad (7)$$

$$G_m = \frac{5-4\nu}{5(2-\nu)} \sqrt[3]{\frac{3C^2(1-\phi)^2 G_0^2}{2\pi^2(1-\nu)^2} P_{eff}}, \quad (8)$$

where C is the grain coordination number, G_0 is the shear modulus of soil grains, ν is the Poisson's ratio of the soil grains, and P_{eff} is the effective stress. To accurately predict velocity in shallow unconsolidated sediments, we incorporate the net overburden pressure $\sigma - u_a$, matric suction $u_a - u_w$, and cohesion σ_{co} in the estimation of effective stress P_{eff} (Lu and Likos, 2006):

$$P_{eff} = \sigma - u_a - S_e(u_a - u_w) + \sigma_{co}, \quad (9)$$

where σ is the overburden pressure and equals $\rho_{bulk} gh$ (where ρ_{bulk} is the bulk density of soil with pore fluids, g is the gravitational acceleration, and h is the depth of soil); u_a is the atmospheric pressure; σ_{co} is the cohesion and can be up to 300 kPa in sand; and $S_e(u_a - u_w)$ is the matric suction contribution weighted by the effective water saturation S_e (Song et al., 2012). At equilibrium, matric suction $u_a - u_w$ equals the weight of the water column. Water saturation S_w is related to S_e as (van Genuchten, 1980)

$$S_w = \frac{S_e(\phi - \theta_r) + \theta_r}{\phi}, \quad (10)$$

where θ_r is the residual volumetric water content. Volumetric water content θ can be converted to water saturation S_w by: $S_w = \theta/\phi$, where θ is the volumetric water content.

The Wood and Hill averages

The Wood (1941) average estimates the average bulk modulus of pore fluids (K_{fl}, in equation 5) using a weighted harmonic mean of the bulk modulus of each pore fluid (Mavko et al., 2009):

$$K_{fl} = \left(\sum_i \frac{f_i}{K_{fl_i}}\right)^{-1}, \quad (11)$$

where f_1 is the volumetric fraction of the individual fluid and K_{fl_i} is the individual fluid's bulk modulus. To apply the Wood average for a scenario in which the pore fluids are water and air, we assume two different water saturations exist, one in the patches (S_{w_1}) and another in the surrounding area (S_{w_2}). The average fluid bulk modulus with patchy saturation (K_{fl}, in equation 5) becomes

$$\frac{1}{K_{fl}} = \frac{S_{w_1} f_1}{K_w} + \frac{(1-S_{w_1}) f_1}{K_a} + \frac{S_{w_2}(1-f_1)}{K_w} + \frac{(1-S_{w_2})(1-f_1)}{K_a}, \quad (12)$$

where f_1 is the volumetric fraction of the pore space in patches with water saturation S_{w_1}, $(1-f_1)$ is the volumetric fraction of the pore space in adjacent area with water saturation S_{w_2}, and K_w and K_a are the bulk modulus of water and air, respectively. In shallow sediments, residual air and water may be trapped in small pore spaces and so the water saturation cannot reach either 0% or 100%.

In a special condition where there is one water saturation value for a given capillary pressure, the Wood average can be simplified to the commonly used averaging method in the Gassmann theory (Gassmann, 1951). In this case, the volumetric fraction (equation 12) of patches is 0% or 100%. Then, the HM-BG model describes a homogeneous saturation pattern. In the Gassmann model, the average fluid bulk modulus (K_{fl}, in equation 5) is simplified to (Mavko et al., 2009)

$$\frac{1}{K_{fl}} = \frac{S_w}{K_w} + \frac{(1-S_w)}{K_a}, \quad (13)$$

where S_w is the water saturation at a fixed capillary pressure. In this case, the HM-BG-Wood model is simplified to the commonly used HM-BG model (Mavko et al., 2009).

The Hill (1963) average determines the average effective bulk and shear moduli (K_{eff} and G_{eff}, in equations 2 and 3) by using a weighted harmonic mean of the effective bulk and shear moduli of each patch:

$$\frac{1}{K_{eff} + \frac{4}{3}G_{eff}} = \sum_i \frac{f_i}{K_{eff_i} + \frac{4}{3}G_{eff_i}}, \quad (14)$$

where f_i is the volumetric fraction of each patch and K_{eff} and G_{eff} are the bulk and shear moduli of the sand matrix with pore fluids in each patch, respectively. In each patch, water is homogeneously distributed. If we assume that there are two different water saturations (S_{w_1} and S_{w_2}) in patches and the surrounding area, then equation 14 becomes

$$\frac{1}{K_{eff} + \frac{4}{3}G_{eff}} = \frac{f_1}{K_{eff_1} + \frac{4}{3}G_{eff_1}} + \frac{(1-f_1)}{K_{eff_2} + \frac{4}{3}G_{eff_2}}, \quad (15)$$

where f_1 is the volumetric fraction of patches with water saturation S_{w_1}, $(1-f_1)$ is the volumetric fraction of the adjacent area with water saturation S_{w_2}, K_{eff_1} and K_{eff_2} are the effective bulk moduli of the sand matrix with pore fluids in patches and in adjacent areas,

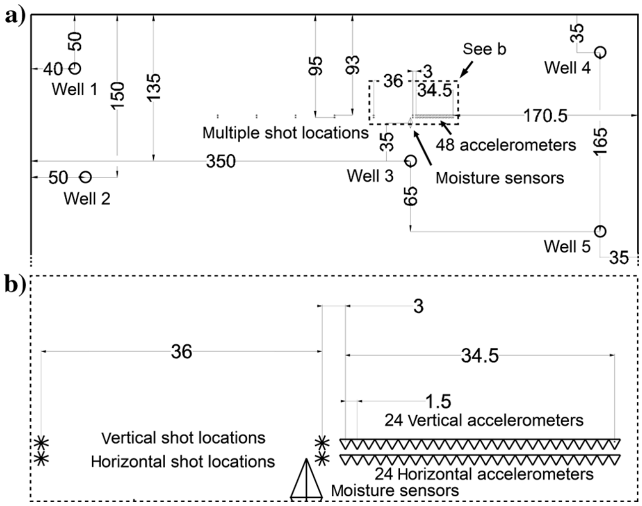

Figure 1. Experiment equipment layout of accelerometers (triangles), shot locations (stars), and moisture sensors (rhombus or half-rhombus). All units are in cm. (a) Sand tank contains five monitoring wells (circles). (b) Magnified portion of (a) within the dashed rectangle (inset).

respectively, and G_{eff_1} and G_{eff_2} are the effective bulk moduli of the sand matrix with pore fluid in patches and in adjacent areas, respectively.

SEISMIC ACQUISITION AND INVERSION

To test our seismic inversion method for fluid-distribution conditions, we conduct a seismic survey during imbibition and drainage experiments in approximately $6 \times 9 \times 0.6$ m sand-filled tank (Figure 1). We collect P- and S-wave pseudo-walkaway seismic data during imbibition at six different WLs (WL1-6, from 0 to 0.46 m), during draining at five different WLs (WL7-11, from 0.46 to 0.02 m), and for a reference test (WL0) in air-dry sand with residual water saturation (Table 1). Each time we change the WL, we wait between 2 and 4 h for the water to reach equilibrium in five monitoring wells (Figure 1a, measured by WL sensors).

A previous imbibition experiment was conducted in the same sand tank with a similar acquisition system, but the sand had at least two layers (Lorenzo et al., 2013). After the previous experiment, we attempted to homogenize sand grains. During homogenization, sand is mixed with shovels into one pile. The sand is spread to cover two-third of the tank in a wedge shape similar to a sandy beach profile. We flattened the highest part of the sand, which is approximately 0.55 m thick and is where the seismic survey is conducted. Homogeneity may be partially limited by the smallest average volume of shoveled sand (approximately $0.15 \times 0.2 \times 0.5$ m).

After homogenization, we conducted a series of laboratory tests on sand properties, such as grain size distribution, porosity, density, and elasticity, on 10 samples we collected from various locations and depths in the sand tank. Sand sieve analysis indicates that there is approximately 5% difference in grain size distribution parameters (Table 2), including mean, sorting (the degree of scatter), skewness (the degree of lopsidedness), and kurtosis (the degree of "tailedness" of the sand-size distribution) (Folk and Ward, 1957). The variations in grain size distribution indicate possible sand heterogeneity, which may lead to heterogeneity in saturation conditions during imbibition and draining. Based on the results from X-ray diffraction analysis, the sand is composed of approximately 98% of quartz, approximately 1% of K-feldspar, and approximately 1% of plagioclase. We use the elasticity of quartz (Mavko et al., 2009) for our velocity prediction (Table 3). From laboratory measurements of sample weight and volume, we also determine bulk density for air-dry sand and porosity for air-dry and wet sand (Table 3).

The seismic acquisition system uses an ultra-high frequency (up to 20 kHz) magnetostrictive vibrator and 48 1C accelerometers (Table 4). The seismic wavelength is approximately 4 cm (with a velocity on the order of 100 m/s and a dominant frequency of approximately 2.5 kHz). At each WL, we collect six shot gathers with a total survey width of 2.17 ± 0.02 m (Figure 1). The

Table 1. WL height values measured from the bottom of the sand and water depth values from the top of the sand (the thickness of the sand is approximately 0.55 m).

WL	WL height from sand bottom (m)	Depth from sand top (m)	WL	WL height from sand bottom (m)	Depth from sand top (m)
WL0	0	0.55	WL6	0.46	0.09
WL1	0.07	0.48	WL7	0.35	0.2
WL2	0.2	0.35	WL8	0.27	0.28
WL3	0.29	0.26	WL9	0.19	0.36
WL4	0.36	0.19	WL10	0.13	0.42
WL5	0.40	0.15	WL11	0.02	0.53

Table 2. Statistical parameters of grain size by sand sieve analysis for 10 samples from various (random) locations and depths in the sand tank after "homogenization." The grain size parameters show variations in mean, sorting, skewness, and kurtosis.

Sample	Mean (mm)	Mean (phi)	Sorting	Skewness	Kurtosis
1	0.3393039	1.55935	0.50271	−0.05406	1.00922
2	0.3338287	1.58282	0.49264	−0.04258	1.04724
3	0.3422802	1.54675	0.52116	−0.063	1.02432
4	0.3473495	1.52554	0.497	−0.02641	0.97075
5	0.3571915	1.48523	0.54523	−0.14979	1.01593
6	0.3456107	1.53278	0.50482	−0.04576	0.99724
7	0.3372943	1.56792	0.49256	−0.04177	1.02035
8	0.3412048	1.55129	0.49328	−0.03972	1.00075
9	0.3403544	1.55489	0.4877	−0.04146	0.98799
10	0.3447350	1.53644	0.48772	−0.03827	0.98525

vibration source is oriented vertically and horizontally. In total, 24 accelerometers are buried (3 cm depth) in one row and oriented with the most sensitive axis parallel to source vibration direction. Another 24 accelerometers are buried (also at 3 cm) in another row and oriented with the most sensitive axis orthogonally to the source, hence they can capture SH-waves (Figure 1b). The accelerometers are placed 1.5 cm apart (center to center) for a total array length of 34.5 ± 0.2 cm. There are a total of six shots for each pseudo-walkaway survey. The first shot offset is 3 cm (center to center), and each subsequent shot location is moved 36 cm (Figure 1b).

To determine V_P and V_S-versus-depth profiles, we attempt to best match the traveltimes of refracted and reflected first arrivals of P- and S-waves by forward-tracing rays (Cerveny, 2001) with 1D gradient-velocity layers (shown with P-wave examples in Figure 2). The thickness of each velocity layers can also be determined with forward ray-tracing modeling. For postcritically refracted rays, velocity values over any given depth range are associated with material properties that lie halfway, horizontally, between source and receiver. Averaging may occur, but only within each given constant- or constant-gradient-velocity depth interval.

During processing, seismic amplitudes are rebalanced through division by the root-mean-square (rms) average at each recorded accelerometer with a window width of 0.002 s. Band-pass frequency filtering between 200 and 5000 Hz is applied to suppress noise. In Figure 2, the straight or slightly concave-upward seismic events correspond to P-wave refractions within the sand body (higher slope) and from the concrete bottom of the tank (lower slope). The higher slope refraction arrivals can be best matched by two velocity layers with distinct gradients, whereas the lower slope arrivals can be best matched by a constant velocity approximately 2000 m/s. The concave-downward seismic arrival approximately 0.008 s is interpreted to correspond to a P-wave reflection from the bottom of the sand tank and can be best matched by a sharp velocity increase from approximately 150 to 2000 m/s. We set the P-wave velocity scale from approximately 110 to 180 m/s in Figure 2 to show velocity changes in sands, hence the velocity layer (approximately 2000 m/s) for the concrete bottom of the tank could not be shown. The V_P-versus-depth profile from WL2 is also representative of WL1-3, and the profile from WL 4 is representative for WL0, 4, 5, and 7-11. S-wave refraction arrivals, which have a straight or slightly concave-upward shape, can be best matched by a single layer showing a consistent-velocity gradient. S-wave refraction arrivals have a larger slope than P-wave refraction but similar to Rayleigh wave refraction arrivals in Figure 2. S-wave reflections that have a concave-downward shape are interpreted to reflect from the bottom of the sand tank. Compared with V_P, V_S is less sensitive to changes in water saturation and depth. Velocity profiles represent average velocities within each layer over the seismic survey width (2.17 m). The error in velocity is less than $\pm 2\%$ (from $\pm 10^{-4}$ s error in traveltime). We extract V_P and V_S at the depths of 0.1 and 0.37 m from V_P- and V_S-versus-depth profiles (Figure 2) to show velocity changes with various WLs and water saturations at a given depth (Figure 3). These depths are chosen to represent the central portion of two zones with distinct velocity gradients (Figure 2).

To show changes in seismic velocity with water saturation and verify inverted saturation results, we also measure volumetric water content during experiments with five moisture sensors buried horizontally in the sand at different depths (0.1, 0.19, 0.28, 0.37, and 0.46 m). These capacitance-/frequency-domain sensors detect the volumetric water content by measuring the dielectric constant of the sand (Table 4). The readings from moisture sensors are collected for 90 s (at the rate of 1 sample/s) each time after the WL reaches equilibrium and before seismic acquisition. We self-calibrate the sensors by determining a linear relationship between the sensor's voltage readings and volumetric water content measured from gravimetric sampling methods using oven drying (Dane and Topp, 2002; Czarnomski et al., 2005) for air-dry and wet sands in the sand tank. The volumetric water content is calculated with the self-calibrated linear relationship from the average voltage of the

Table 3. Key parameters with known values from Mavko et al. (2009) and laboratory measurements used for velocity estimation.

Parameters	Values	Parameters	Values
g (m/s^2)	9.80665	K_0 (Pa)	3.66×10^{10}
ρ_w (kg/m^3)	1	G_0 (Pa)	4.5×10^{10}
ρ_a (kg/m^3)	1.18×10^{-3}	ρ_0 (kg/m^3)	2.65
K_w (Pa)	2.2×10^9	ρ_{eff} (dry, kg/m^3)	1.54
K_a (Pa)	1.01×10^5	ϕ (wet)	0.4
C	3	ϕ (dry)	0.43

Table 4. Descriptions for the seismic, moisture, and WL acquisition equipment used in our experiments. More details for the seismic acquisition system are described by Lorenzo et al. (2013).

Equipment	Description
Accelerometer	48 piezoelectric accelerometers (ACH01 from Measurement Specialties Inc.); linear response in 2–20 kHz range with sensitivity of 10 mV/g.
Vibration source	Magnetostrictive ultrasonic transducer (Model CU-18 from Etrema Products Inc.); the source wavelet is a Ricker wavelet with a vibration frequency up to 20 kHz and a central frequency at 10 kHz.
Moisture sensor	Five capacitance/frequency-domain sensors (EC-5 from Decagon Devices Inc.); the maximum measurement volume is 240 ml for a cylindrical volume with a radius of approximately 3 cm and a height of approximately 10 cm; the accuracy is $\pm 2\%$; the resolution is 0.001 m^3/m^3; the measurement range is from zero to saturation; the operating temperature is −40 to 60°C.
WL sensor	Five submersible pressure transducers (WL400 from Global Water Instrumentation Inc.); the accuracy is $\pm 0.1\%$; the operating temperature is −40 to 85°C.

90 s voltage readings. Then, we plot the observed seismic velocity against water saturation at depths of 0.1 and 0.37 m (Figure 4).

To determine fluid-distribution conditions, we use rock-physics models with different fluid distribution assumptions to best match experimental V_P and V_S-versus-depth profiles (Figure 5). We begin our inversion by inputting elasticity values for quartz sand (Mavko et al., 2009) and values for porosity and bulk density of air-dried sand, derived from samples in the sand tank. These known property values help to constrain inverted results and accelerate the inversion (Table 3). The inversion results include SWCC, S_w, and the volumetric fraction of the patches (Figure 5). We minimize the misfit between experimental and predicted V_P and V_S-versus-depth profiles for each WL, aided by the covariance matrix adaptation evolution strategy optimization (Shen et al., 2015). The best fit for the experimental data relies on the lowest rms misfit to arrive at the preferable inversion result. Like the effective bulk modulus, the effective shear modulus is averaged according to equations 12 and 15 as well. As V_P is more sensitive to water saturation changes than V_S, inverted SWCC and saturation results depend on mostly on V_P-versus-depth profiles. Velocity prediction models are based on the HM-BG model, but have three different averaging methods depending on their respective fluid distribution assumptions: (1) HM-BG for homogeneous saturation (average using equation 13), (2) HM-BG-Wood for small-sized patchy saturation (average using equa-

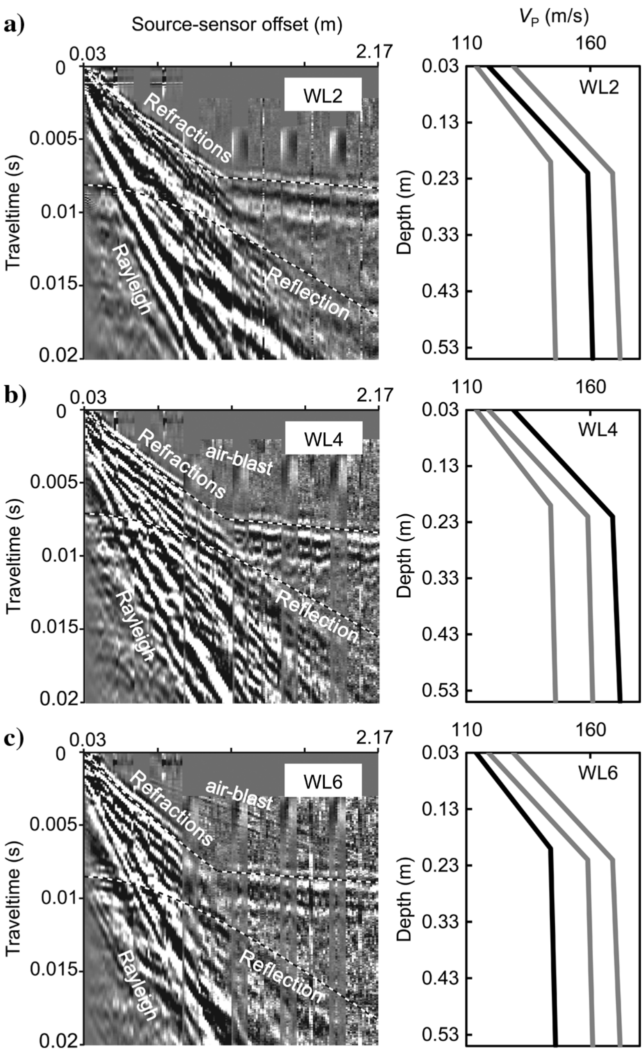

Figure 2. Representative seismic data sets and interpreted V_P-versus-depth profiles at different WLs: (a) WL2, (b) WL4, and (c) WL6. On the left, variable-area plots display seismic amplitudes interpolated among shades of gray with positive seismic amplitudes in black and negative amplitudes in white. Synthetic seismic events, forward modeled using the first arrivals of refracted and reflected rays (dashed lines) are drawn over seismic panels. The V_P-versus-depth profiles used to calculate distance-traveltime locations for seismic rays are shown highlighted with solid black lines to the right of each data set. The solid gray lines are other velocity profiles to show how velocity profile changes with WL. Key seismic arrivals in data are labeled near calculated synthetic events.

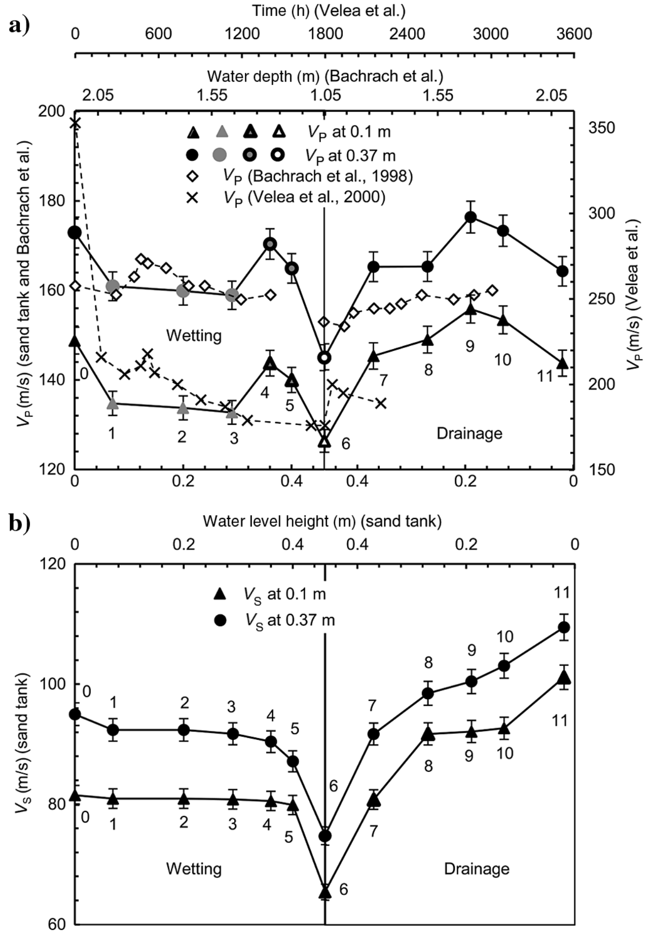

Figure 3. The V_P and V_S-WL relationships during imbibition and draining. (a) V_P values in the sand tank (this paper) from depths of 0.1 (differently shaded triangles) and 0.37 m (differently shaded circles). Also shown for comparison are V_P values from Bachrach and Nur (1998) (as rhombi) and V_P values from Velea et al. (2000) (as crosses). (b) V_S values in the sand tank (this paper) from depths of 0.1 (solid black triangles) and 0.37 m (solid black circles). The top horizontal WL axis shows water depths measured from the top of the sand (Bachrach and Nur, 1998), whereas the bottom axis shows WL height measured from the bottom of the sand in the sand tank (this paper). WL0–11 (this paper) is labeled as "0–11." Velocities are grouped into four cases: WL1–WL3 (solid gray circles and triangles), WL4, WL5 (gray circles and triangles with black outline), WL6 (hollow circles and triangles), and WL7–WL11, WL0 (solid black circles and triangles).

tion 12), and (3) HM-BG-Hill for large-sized patchy saturation (average using equation 15).

RESULTS

The V_P-WL (Figures 3a) and V_P-S_w (Figures 4) relationships are nonmonotonic in the shallow (represented by the depth at 0.1 m) and deep (represented by the depth at 0.37 m) sand. No general trend can be observed throughout the imbibition or drainage. During imbibition, V_P values oscillate from peak to trough twice. The peaks of the V_P value occur in air-dry sand (WL0) and WL4. V_P reaches the lowest value at the highest WL and water saturation (WL6). During drainage, the V_P-WL relationship has a transition between increasing and decreasing trends, and the peak of the V_P value occurs at WL9 (Figure 3a).

In contrast to the nonmonotonic V_P-WL relationship, the V_S-WL relationship is monotonic during the imbibition and drainage of the sand (Figure 3b). V_S values decrease throughout the imbibition (WL1-6) and increase throughout the drainage (WL7-11).

Based on the inversion results and the V_P-versus-depth profiles among 12 WLs (WL0–WL11), we distinguish four representative cases for four different groups to summarize the results (Figure 3). V_P-versus-depth profiles and inversion results differ by less than ±3% within each case and larger than 7% in different cases.

(Case 1) During the earliest stage of imbibition (WL1-3, represented by WL2), velocity-versus-depth profiles are best fit by the HM-BG-Wood model (Figure 6a). (Case 2) During the middle stage of imbibition (WL4 and WL5, represented by WL4), velocity-versus-depth profiles are best fit by the HM-BG-Hill model (Figure 6b). (Case 3) When WL is the highest (WL6), velocity-versus-depth profiles are best fit by the HM-BG-Wood and the HM-BG models (Figure 6c). (Case 4) During draining (WL7-11, WL0, represented by WL10), velocity-versus-depth profiles are best fit by the HM-BG-Hill model (Figure 6d).

The quality for the inversion results can be shown by the good correlation between inverted water saturation with measured in situ water saturation. Average measured water saturation for each V_P value in the sand tank is calculated using arithmetic average of the water saturation at each depth. The inverted water saturation agrees with the measured water saturation with a difference of less than 7% for all WLs (Figure 7). The error is ±2% in measured water saturation (from instrument error). The inverted water saturation has an error of ±10%, which is determined using a Monte Carlo method after 100 inversion attempts (Shen et al., 2015). The difference between inverted and measured water saturation is within the error of the inverted water saturation.

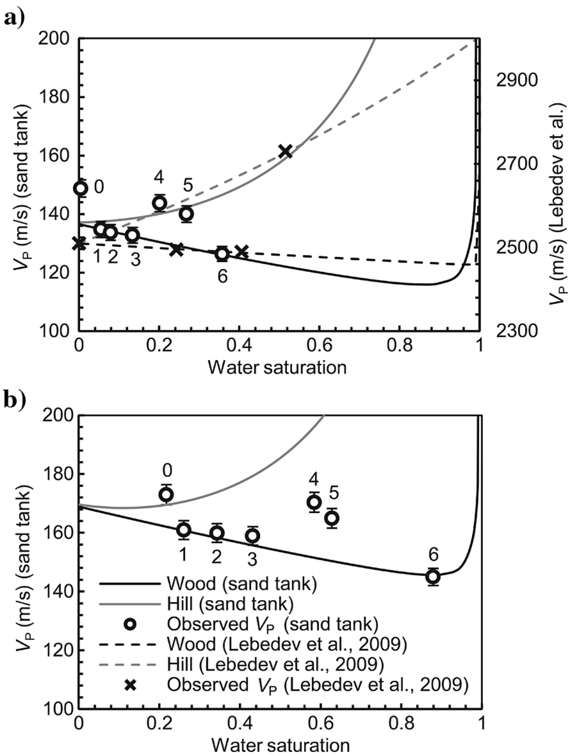

Figure 4. The V_P-S_w relationships during imbibition. (a) V_P values (as hollow circles) come from the sand tank at the depth of 0.1 m (this paper). Also shown for comparison are V_P values (as crosses) come from observations in sandstone core samples (Lebedev et al., 2009). The vertical axis for V_P in the sand tank (this paper) is on the left, whereas for the sandstone core (Lebedev et al., 2009) is on the right. Theoretical HM-BG-Hill and HM-BG-Wood bounds for unconsolidated sands in this paper are shown by gray and black solid lines, respectively. Theoretical HM-BG-Hill and HM-BG-Wood bounds for sandstone (Lebedev et al., 2009) are shown by gray and black dashed lines, respectively. (b) V_P values (as hollow circles) come from the sand tank at the depth of 0.37 m (this paper). WL0–6 are labeled as "0–6."

DISCUSSION

Although our experiment is conducted once, similar observed nonmonotonic V_P-WL relationships have been described in a laboratory test with Ottawa Sand (Velea et al., 2000) and tidal experiments at a sandy beach (Bachrach and Nur, 1998) (Figure 3a). Consistent with the observations made by Bachrach and Nur (1998) and Velea et al. (2000), there are two oscillations in V_P values during imbibitions, and the V_P value is the lowest at the highest WL. During drainage, the transition from an increasing to a decreasing trend in our V_P-WL relationship is in agreement with the observation made by Velea et al. (2000) (Figure 3a). However, Bachrach and Nur (1998) only observe an increasing trend during the drainage (Figure 3a). The different observations are attributed to the differences in sediment heterogeneity and experiment setup (e.g., seismic frequency, injection rate, and the density and viscosity of pore fluids) (Homsy, 1987). One possible

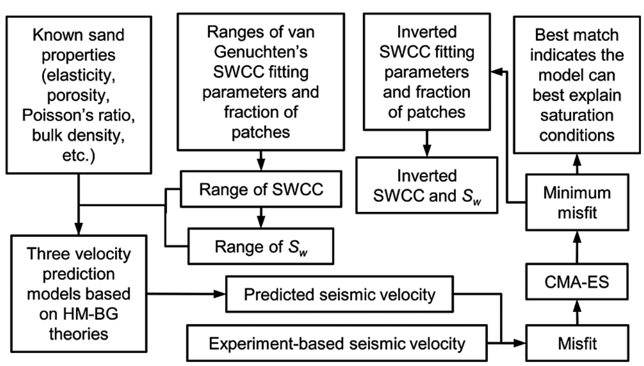

Figure 5. Workflow chart for the inversion process shows input and output parameters. Three velocity prediction models include the HM-BG, HM-BG-Wood, and HM-BG-Hill models. CMA-ES is the optimization program used to minimize misfit.

explanation for the difference is that the time durations of the two drainage processes are different: the drainage in our experiment lasts for approximately 15 h, whereas in Bachrach and Nur (1998)'s, it lasts approximately 2 h. As a result, their experiment may not have captured the decreasing trend in V_P-WL relationship during the drainage.

The nonmonotonic V_P-S_w relationship can be explained by the transitions between the HM-BG-Wood and the HM-BG-Hill bounds, depending on the change in patch size (Lebedev et al., 2009) and seismic frequency (Cadoret et al., 1995). We interpret that the transitions in V_P-S_w relationships between the HM-BG-Wood and the HM-BG-Hill bounds are attributed to the variation in the patch size relative to the diffusion length (Figures 4 and 6). At low water saturation (WL1-3), the V_P-S_w relationship follows the HM-BG-Wood bound (Figures 4 and 6a). We interpret that the patches are small sized (<1 cm) at the beginning of imbibition. When the inverted average water saturation (arithmetic mean) is more than approximately 45% (WL4, Figure 7b), V_P values have a transition from the HM-BG-Wood to HM-BG-Hill bound (Figures 4a and 6b) or between the two bounds (Figures 4b and 6b). We interpret that the large-sized patches (>1 cm) start to form during the middle stage of imbibition. When WL is the highest (WL6), V_P values have a transition from the HM-BG-Hill back to the HM-BG-Wood bound (Figures 4 and 6c). We interpret that the water distribution is relatively homogeneous with small-sized residual-air patches at the highest WL. During drainage, the V_P-S_w relationship follows the HM-BG-Hill behavior (Figure 6d), and this result is in agreement with previous laboratory observations (Murphy, 1982; Knight and Nolen-Hoeksema, 1990; Cadoret et al., 1995; Monsen and Johnstad, 2005;). We interpret that the patches are large sized (>1 cm) during drainage.

The transition from HM-BG-Wood behavior to HM-BG-Hill behavior (WL1–WL5) is consistent with a previous laboratory study, which shows that the transition happens when small patches cluster as water saturation exceeds 40% (Figure 4) (Lebedev et al., 2009). During injection of water into a sandstone sample, Lebedev et al.

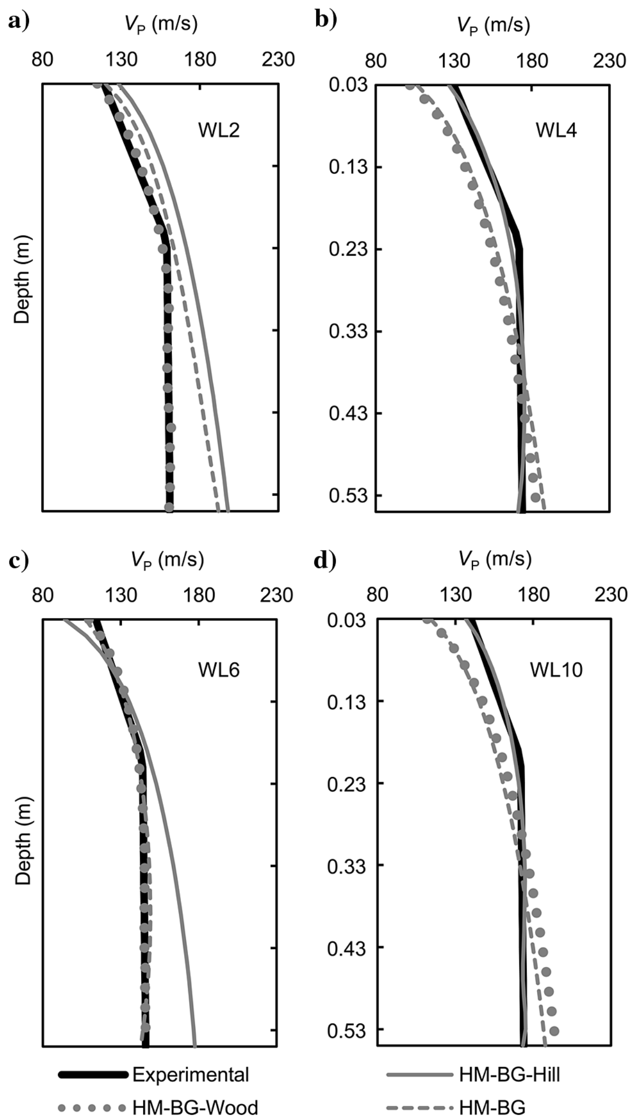

Figure 6. A comparison between representative experimental V_P-versus-depth profiles (in solid black lines) and inverted V_P-versus-depth profiles using the HM-BG (in solid gray lines), the HM-BG-Hill (gray dashed lines), and the HM-BG-Wood (gray dotted lines) models for (a) WL2, which is representative of inversion results for WL1–3 and is best fit by the HM-BG-Wood model, (b) WL4, which is representative of inversion results for WL0, 4, and 5 and is best fit by the HM-BG-Hill model, (c) WL6, which is best fit by the HM-BG and HM-BG-Wood models, and (d) WL10, which is representative of inversion results for WL7–11 and is best fit by the HM-BG-Hill model.

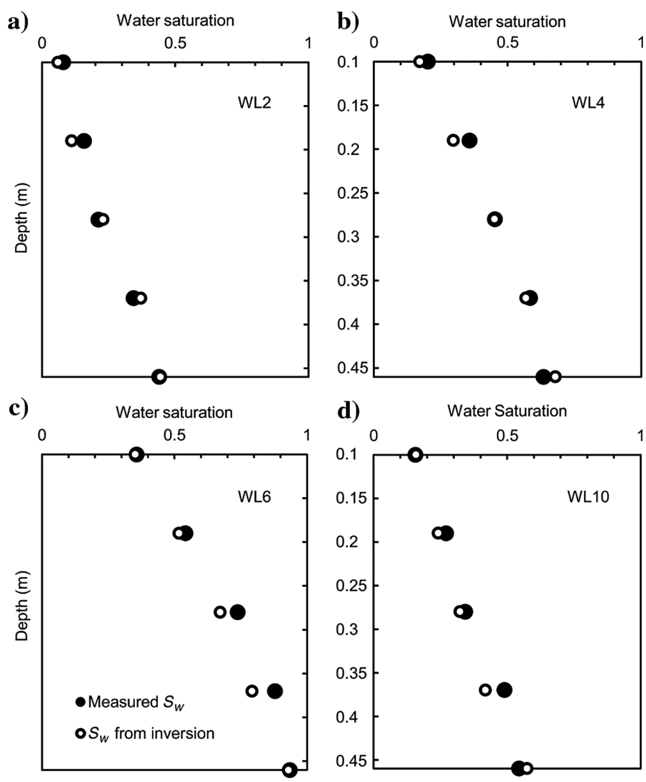

Figure 7. A comparison of representative water saturation-depth profiles from inversion (hollow circles) and measurements by moisture sensors (black solid circles) at different WLs: (a) WL2, (b) WL4, (c) WL6, and (d) WL10. Measured water saturation is calculated from measured volumetric water content. The inverted water saturation is an average from S_{w1} and S_{w2} and weighted by f_1 (in equations 12 and 15).

(2009) observe that V_P decreases slightly and follows the HM-BG-Wood bound at low water saturations. When water saturation exceeds approximately 40%, V_P sharply increases and can be interpreted by a transition from the HM-BG-Wood to HM-BG-Hill bound. Their results from X-ray computer tomography show that the interpreted transition from the HM-BG-Wood to HM-BG-Hill bound corresponds to the clustering of small fluid patches and the formation of larger patches. Some observations show that the experimental V_P-S_w relationship can be explained by the lower velocity bound from the HM-BG-Wood model during imbibition, and the upper velocity bound from the HM-BG-Hill model during drainage (Murphy, 1982; Knight and Nolen-Hoeksema, 1990; Cadoret et al., 1995; Monsen and Johnstad, 2005).

The assumptions behind each rock-physics model can be used to interpret the fluid-distribution condition at WLs. When the HM-BG-Wood model best describes the velocity-versus-depth profiles (WL1-3; Figures 4 and 6a), it suggests that the patch sizes are small in comparison with the diffusion length (approximately 1 cm in our unconsolidated sands) at the beginning of the imbibition. However, when the HM-BG-Hill model provides a better fit to the velocity-versus-depth profile, we can interpret that the size of the patches is larger than the diffusion length (>1 cm) (WL0, 4, 5, 7–11; Figures 4, 6b, and 6d). In the air-dry sand (WL0), the matric suction contribution weighted by water saturation (equation 9) is minimum and so the effective pressure is highest. The high effective pressure may also lead to the relatively high V_P value. At WL6 (highest), the best fit by HM-BG and HM-BG-Wood models indicates that the saturation condition is homogeneous (Figures 4 and 6b). For WL6, the inversion results from HM-BG-Wood show that no patches exist.

Based on the interpretation of the patch size during the imbibition and draining, we can also infer a model for the development of fluid-distribution conditions at different WLs/saturations (Figure 8). At the beginning of imbibition, small-sized patches are formed because of large capillary forces at low saturation (Lopes et al., 2014). Capillary fingers rise higher along small pore throats in which the capillary pressure is greatest (Figure 8a). When the water saturation is more than 45%, capillary fingers start to cluster and form large-sized patches as water migrating from large pores to small pores. After water redistribution, water saturations are higher in the sand patches with higher permeability and porosity (Figure 8b). The size of large patches is likely comparable with the size of the shovel-sized patches in the sand tank (approximately 0.15×0.2 m). When the WL almost reaches the top of the sand, large patches are connected and so water is distributed homogeneously, but residual air may be trapped in small pore space when pore pressure dropped below irreducible air pressure (Figure 8c) (Faybishenko, 1995). During the drainage, large-sized patches remain because no capillary finger can be formed during drainage owing to the hydrophilic nature of the sand. Water tends to drain from sand patches with higher permeability and porosity first, and residual water may be trapped in patches with less permeability and porosity. At the end of drainage (in air-dry sand), large patches with less permeability and porosity end up with higher residual water saturation compared with the patches with higher permeability and porosity.

Alternative interpretations could exist if the capillary rise and fringe and near-fully saturated zones were homogeneous and layered, and seismic waves traveled only at the interface between unsaturated and near-fully saturated zones. However, measured and inverted water saturation data show that water saturation values are below 95% throughout the sand even when the WL almost reaches the top of the sand (Figure 7). Experimental-based P-wave velocities that are between 80 and 230 m/s (Figure 2) also indicate the sand is below full saturation, as V_P usually reaches approximately 1500 m/s in fully saturated sands. One possible reason is that some amount of air remains trapped within the smaller pores of unconsolidated sands. Similar results are observed in a previous sand tank experiment (Lorenzo et al., 2013).

Our research focuses on shallow unconsolidated sands, however, the approach and analysis used in this research to determine fluid-saturation conditions may also be applicable for deeper sediments. Seismic frequency is scaled in our experiment for shallow sediments. Frequencies in shallow seismic data are usually much higher than frequencies in deeper sediments (approximately 0–100 Hz). One difference between deeper and shallow sediments is effective stress, which can be dominated by overburden pressure for deeper sediments but may be largely affected by capillary pressure and cohesion at shallow depth. When injecting water into an oil reservoir, viscous forces can be dominant compared with capillarity and gravitation (Lopes et al., 2014).

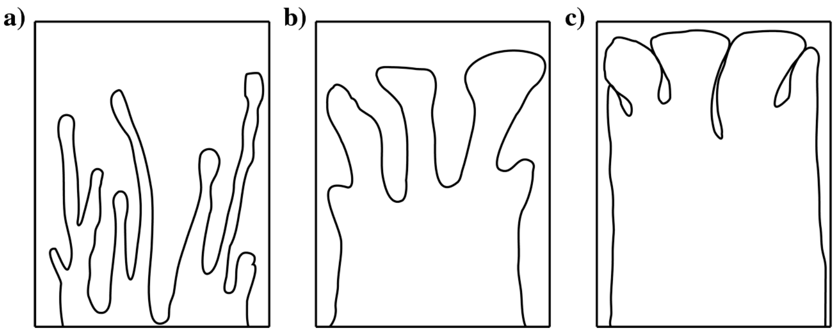

Figure 8. Illustrations of the inferred development in the size of patches as WL (or water saturation) increases for (a) at low saturation, small-sized patches are formed due to capillary fingering effect, (b) when water saturation >45%, large-sized patches are formed from the clustering of small fingers, and (c) when WL almost reaches the top of the sand, small residual-air patches are trapped in small pore spaces as large water patches connect. The sketches can represent sands in the middle part of the tank, where "wall effects" (Velea et al., 2000) are negligible.

CONCLUSIONS

In situ fluid-distribution conditions can be derived by the inversion of V_P and V_S-versus-depth profiles using the HM-BG model with different averaging methods depending on the assumption related with a particular fluid-distribution condition. The inverted water saturation matches the measured water saturation with an error less than 7%.

The observed nonmonotonic V_P-WL relationship from water-level change experiments is best explained by alternating between the HM-BG-Wood and HM-BG-Hill bounds, and we interpret the alternations are possibly caused by the variation in patch size during the imbibition and draining of the sand. At low water saturation, V_P values follow the HM-BG-Wood bound that indicates small-sized patches are possibly formed because of capillary fingering effect. When water saturation is more than 45%, V_P-S_w relationship shows a transition from the HM-BG-Wood to the HM-BG-Hill bound, and we interpret the transition as caused by a change in patch size from small to large. When WL almost reaches the top of the sand, the V_P-S_w relationship shows a transition from the HM-BG-Hill back to the HM-BG-Wood bound, and we interpret this transition as caused by a change from large water-saturated patches to small-sized residual-air patches. During drainage, V_P values follow the HM-BG-Hill bound that indicates the patches are large sized because no capillary finger can be formed due to the hydrophilic nature of the sand.

ACKNOWLEDGMENTS

This work is supported by a Shell Exploration & Production Company Grant (2011–2015). We would like to thank F. Tsai and H. Pham for their help with optimization techniques, L. Butler and A. Brooks for their help with Labview programming, Ario Labs in Baton Rouge for their help with building the seismic acquisition system, C. Gama for her help with grain size analysis, and R. Young and C. Li for the support with facilities and the sand tank. We thank the following for their support with scholarships to the first author: Geometrics Inc. Student Travel Grant for SAGEEP, the Donald Towse Memorial Fund awarded by AAPG Grant-in-Aid, H. V. Anderson Scholarship, EnCana Scholarship and Imagine Resources Scholarship awarded by the LSU Department of Geology and Geophysics, and especially to the LSU Department of Geology and Geophysics for their active support of graduate student research.

REFERENCES

Bachrach, R., and A. Nur, 1998, High-resolution shallow-seismic experiments in sand, Part I: Water table, fluid flow, and saturation: Geophysics, **63**, 1225–1233, doi: 10.1190/1.1444423.

Biot, M. A., 1962, Mechanics of deformation and acoustic propagation in porous media: Journal of Applied Physics, **33**, 1482–1498, doi: 10.1063/1.1728759.

Cadoret, T., D. Marion, and B. Zinszner, 1995, Influence of frequency and fluid distribution on elastic wave velocities in partially saturated limestones: Journal of Geophysical Research: Solid Earth, **100**, 9789–9803, doi: 10.1029/95JB00757.

Cadoret, T., G. Mavko, and B. Zinszner, 1998, Fluid distribution effect on sonic attenuation in partially saturated limestones: Geophysics, **63**, 154–160, doi: 10.1190/1.1444308.

Cerveny, V., 2001, Seismic ray theory: Cambridge University Press.

Czarnomski, N. M., G. W. Moore, T. G. Pypker, J. Licata, and B. J. Bond, 2005, Precision and accuracy of three alternative instruments for measuring soil water content in two forest soils of the Pacific Northwest: Canadian Journal of Forest Research, **35**, 1867–1876, doi: 10.1139/x05-121.

Dane, J. H., and G. C. Topp, 2002, Methods of soil analysis: Part 4. Physical methods: Soil Society of America.

DiCarlo, D. A., 2003, Drainage in finite-sized unsaturated zones: Advances in Water Resources, **26**, 1257–1266, doi: 10.1016/j.advwatres.2003.09.001.

Dvorkin, J., and A. Nur, 1998, Acoustic signatures of patchy saturation: International Journal of Solids and Structures, **35**, 4803–4810, doi: 10.1016/S0020-7683(98)00095-X.

Faybishenko, B. A., 1995, Hydraulic behavior of quasi-saturated soils in the presence of entrapped air: Laboratory experiments: Water Resources Research, **31**, 2421–2435, doi: 10.1029/95WR01654.

Folk, R. L., and W. C. Ward, 1957, Brazos River bar: A study in the significance of grain size parameters: Journal of Sedimentary Research, **27**, 3–26.

Gassmann, F., 1951, Elastic waves through a packing of spheres: Geophysics, **16**, 673–685, doi: 10.1190/1.1437718.

Hertz, H., 1882, On the contact of rigid elastic solids and on hardness, chapter 6: Assorted papers by H. Hertz: MacMillan.

Hill, R., 1963, Elastic properties of reinforced solids: Some theoretical principles: Journal of the Mechanics and Physics of Solids, **11**, 357–372.

Homsy, G. M., 1987, Viscous fingering in porous media: Annual Review of Fluid Mechanics, **19**, 271–311, doi: 10.1146/annurev.fl.19.010187.001415.

Knight, R., J. Dvorkin, and A. Nur, 1998, Acoustic signatures of partial saturation: Geophysics, **63**, 132–138, doi: 10.1190/1.1444305.

Knight, R., and R. Nolen-Hoeksema, 1990, A laboratory study of the dependence of elastic wave velocities on pore scale fluid distribution: Geophysical Research Letters, **17**, 1529–1532, doi: 10.1029/GL017i010p01529.

Lebedev, M., J. Toms-Stewart, B. Clennell, M. Pervukhina, V. Shulakova, L. Paterson, T. M. Müller, B. Gurevich, and F. Wenzlau, 2009, Direct laboratory observation of patchy saturation and its effects on ultrasonic velocities: The Leading Edge, **28**, 24–27, doi: 10.1190/1.3064142.

Lopes, S., M. Lebedev, T. M. Müller, M. B. Clennell, and B. Gurevich, 2014, Forced imbibition into a limestone: Measuring P-wave velocity and water saturation dependence on injection rate: Geophysical Prospecting, **62**, 1126–1142, doi: 10.1111/1365-2478.12111.

Lorenzo, J. M., D. E. Smolkin, C. White, S. R. Chollett, and T. Sun, 2013, Benchmark hydrogeophysical data from a physical seismic model: Computers & Geosciences, **50**, 44–51, doi: 10.1016/j.cageo.2012.07.034.

Løvoll, G., Y. Méheust, K. J. Måløy, E. Aker, and J. Schmittbuhl, 2005, Competition of gravity, capillary and viscous forces during drainage in a two-dimensional porous medium, a pore scale study: Energy, **30**, 861–872, doi: 10.1016/j.energy.2004.03.100.

Lu, N., and W. J. Likos, 2006, Suction stress characteristic curve for unsaturated soil: Journal of Geotechnical and Geoenvironmental Engineering, **132**, 131–142, doi: 10.1061/(ASCE)1090-0241(2006)132:2(131.

Mavko, G., T. Mukerji, and J. Dvorkin, 2009, The rock physics handbook: Tools for seismic analysis of porous media: Cambridge University Press.

Mindlin, R. D., 1949, Compliance of elastic bodies in contact: Journal of Applied Mechanics, **16**, 259–268.

Monsen, K., and S. Johnstad, 2005, Improved understanding of velocity–saturation relationships using 4D computer-tomography acoustic measurements: Geophysical Prospecting, **53**, 173–181, doi: 10.1111/j.1365-2478.2004.00464.x.

Müller, T. M., B. Gurevich, and M. Lebedev, 2010, Seismic wave attenuation and dispersion resulting from wave-induced flow in porous rocks — A review: Geophysics, **75**, no. 5, 75A147–175A164, doi: 10.1190/1.3463417.

Murphy, W. F., 1982, Effects of partial water saturation on attenuation in Massilon sandstone and Vycor porous glass: The Journal of the Acoustical Society of America, **71**, 1458–1468, doi: 10.1121/1.387843.

Norris, A. N., 1993, Low-frequency dispersion and attenuation in partially saturated rocks: The Journal of the Acoustical Society of America, **94**, 359–370, doi: 10.1121/1.407101.

Riaz, A., G.-Q. Tang, H. A. Tchelepi, and A. R. Kovscek, 2007, Forced imbibition in natural porous media: Comparison between experiments and continuum models: Physical Review E, **75**, 036305, doi: 10.1103/PhysRevE.75.036305.

Shen, J., J. M. Lorenzo, C. D. White, and F. Tsai, 2015, Soil density, elasticity, and the soil-water characteristic curve inverted from field-based seismic P-and S-wave velocity in shallow nearly saturated layered soils: Geophysics, **80**, no. 3, WB11–WB19, doi: 10.1190/geo2014-0119.1.

Song, Y.-S., W.-K. Hwang, S.-J. Jung, and T.-H. Kim, 2012, A comparative study of suction stress between sand and silt under unsaturated conditions: Engineering Geology, **124**, 90–97, doi: 10.1016/j.enggeo.2011.10.006.

Toms-Stewart, J., T. M. Müller, B. Gurevich, and L. Paterson, 2009, Statistical characterization of gas-patch distributions in partially saturated rocks: Geophysics, **74**, no. 2, WA51–WA64, doi: 10.1190/1.3073007.

van Genuchten, M. T., 1980, A closed-form equation for predicting the hydraulic conductivity of unsaturated soils: Soil Science Society of America Journal, **44**, 892–898, doi: 10.2136/sssaj1980.03615995004400050002x.

Velea, D., F. D. Shields, and J. M. Sabatier, 2000, Elastic wave velocities in partially saturated Ottawa sand: Soil Science Society of America Journal, **64**, 1226–1234, doi: 10.2136/sssaj2000.6441226x.

Wood, A. B., 1941, A textbook of sound: George Bell & Sons.